Numerical Investigation of Gas-Driven Flow in 2-D Bubble Columns

Y. Pan and M. P. Dudukovic
Dept. of Chemical Engineering, Washington University, St. Louis, MO 63130

M. Chang
Exxon Research and Engineering Company, Florham Park, NJ 07932

Gas-liquid bubbly flow in 2-D bubble columns was studied by numerical simulation. A Eulerian-Eulerian two-fluid model used describes the time-dependent motion of liquid driven by small, spherical gas bubbles injected at the bottom of the columns. Such equations, numerically implemented in this work, were derived by Zhang and Prosperetti. A distinctive feature of this method is the derivation of the disperse-phase momentum equation by averaging the particle (here, the bubble) equation of motion directly, not the macroscopic equation for the particle phase. Both the time-averaged quantities and dynamic characteristics of the macroscopic coherent structures agree with the experimental data of Lin et al. and Mudde et al. The comparison of simulated results with data demonstrates that this physical model and numerical approach can provide the key features of the time-dependent behavior of dispersed bubbly flows qualitatively with reasonable quantitative accuracy. Effects of the number of injectors, magnitude of bubble-induced viscosity, and various parameters in the interphase momentum exchange were also studied by simulating various cases and comparing with measurements. The applicability of different boundary conditions and the sensitivity to the mesh system used are also examined.

Introduction

Bubble column reactors are widely used in the chemical industry due to excellent mass- and heat-transfer characteristics and simple construction. The fundamental properties of the hydrodynamics in bubble columns, which are essential for scale-up and design, are still not fully understood at present mainly due to the complicated nature of multiphase flow. Based on the experimental evidence (such as studies by Tzeng et al. (1993) and Devanathan et al. (1995)), it is clear that, beside the time-averaged quantities, the transient behavior of flow is required to provide proper and needed information on the hydrodynamics and transport parameters in such reactors. For instance, to study the mixing process, one needs the time-dependent velocity field for calculating the convection and turbulent dispersion of a passive scalar in the liquid and/or gas phase.

Correspondence concerning this article should be addressed to M. P. Dudukovic.

The bubble-driven flow in a bubble column is a typical two-phase (gas and liquid) system in which the flow is driven by buoyancy. From the viewpoint of physical modeling, two-phase bubbly flow is commonly defined as a flow pattern in which the gas phase is distributed within a liquid continuum in discrete bubbles much smaller than the characteristic dimension of the container (column diameter). Numerical simulation of two-phase flows either treats the system in an averaged sense as interpenetrating continuum, or explicitly moves bubbles due to the fluid-imposed and body forces—in some cases feeding back the effect of the bubbles on the carrier-fluid motion through various means. The first type of approach is called Eulerian/Eulerian method, while the second is usually referred to as Eulerian/Lagrangian method. In the first approach the two-fluid model is developed to describe the motion for each of the two phases in Eulerian frame of reference. In the second approach, while the continuous phase is still described in Eulerian representation, the dis-

persed phase is instead treated as it is, that is, the discrete bubbles, and each bubble is tracked by solving its equation of motion through the continuous phase.

During the last several years, the dynamic simulation of gas-liquid flow in bubble columns has drawn considerable attention of the investigators in the chemical reaction engineering community. Webb et al. (1992) and Lapin and Lübbert (1994) studied gas-liquid flows in 2-D bubble columns. They used a single-fluid model in which the two-phase flow is regarded as a quasi-single-phase flow with variable density. Bubbles are considered to individually rise in this fluid, thus, leading to a dynamical change of its density which finally results in a convective flow of the bubble/liquid two-phase system. The gas-phase distribution is calculated by either solving the bubble distribution density functions or individually tracking the bubbles or bubble clusters in a Lagrangian frame. A liquid circulation pattern in the columns of low aspect ratio (height to width ratio) has been observed in their simulation. Using an Eulerian/Eulerian model, Sokolichin and Eigenberger (1994) presented a laminar, dynamic 2-D simulation of gas-liquid bubble flow in a flat and uniformly aerated bubble column. In their study, no turbulence model was used in solving the velocity field of the liquid phase and the drag force was calculated with a constant drag coefficient. Their results were further compared with the laboratory observations and data in a 2-D bubble column and loop reactor by Becker et al. (1994). In a series of articles, Delnoij et al. (1997a,b,c) numerically investigated the gas-liquid flow in 2-D bubble columns by Eulerian/Lagrangian methods. The motion of the gas phase was solved by applying either the discrete bubble model or the volume of fluid (VOF) model. Unlike the work by Lapin and Lübbert (1994), where the coupling between the gas and liquid phase was achieved through the effective density of the mixture and no momentum exchange was incorporated, Delnoij et al. (1997a) coupled the two phases by adding a source term, which includes all the forces imposed on the liquid surrounding the bubbles, into the volume-averaged Navier-Stokes equation for the liquid phase. Correspondingly, the gas phase was described by the equations of motion for each individual bubble. Numerical results were compared, mostly in a qualitative way, with the experiments on the partially aerated 2-D bubble column of Becker et al. (1994).

We have witnessed considerable efforts made by using Eulerian/Lagrangian type of simulations, mostly 2-D, for studying the multiphase hydrodynamics in bubble columns. The Eulerian/Lagrangian method is more suitable for fundamental investigations since it allows for direct consideration of various effects related to bubble-bubble and bubble-liquid interaction. The applicability of this method, however, has been and is limited to the situations where the gas velocity and gas holdup are relatively low. In most industrial applications, high gas superficial velocity is used which results in high gas holdup and turbulence (so-called churn turbulent flows). Under such conditions, the Eulerian/Eulerian method is usually preferred. Several challenging issues regarding the modeling of averaged equations and closure relations, which have been the active research topic in the field of multiphase flow for many years, still exist. One key question is how to model the interphase momentum exchange which is related to the problem of calculating the force acting on the bubble and taking into account the effect of multibubble interaction, large deformable bubbles of the disperse phase, and finite value of gas holdup on these forces. Another unresolved issue is modeling of turbulence in two-phase flow.

Turning to the experimental side, the current techniques for studies of multiphase flow include the computer-automated radioactive particle tracking (CARPT) and the particle image velocimetry (PIV). The former is a Lagrangian measurement in which the trajectory of a single particle is recorded. Devanathan et al. (1990) and Yang et al. (1993) have employed this technique to investigate the liquid velocity field in cylindrical bubble columns. The PIV system, which was originally developed for velocity measurement in single-phase flow, has recently been used for multiphase systems under the conditions of low volume fraction of the dispersed phase or in geometries that make the system transparent. This type of measurement for gas-liquid flow in bubble columns has been realized by Chen and Fan (1992) and Chen et al. (1994). Recently, Lin et al. (1996) and Mudde et al. (1997) used PIV and presented their experimental studies of 2-D bubble columns. They provided the detailed measurement of liquid velocity and turbulence intensities for the column of different sizes and under different operating conditions. They also studied the characteristics of the macroscopic flow structures, that is, the central meandering plume and the companion vortical regions, by measuring their frequency, wave length, and moving speed. This information yields a better understanding of the fluid dynamics in a 2-D bubble column and provides a database for further numerical investigations.

It should be noted that most of the previous studies compared the numerical predictions with the experimental measurements in a qualitative manner, while only a few, if any, quantitative comparisons were made. Therefore, although qualitative comparisons seemed satisfactory in general, limited conclusions regarding the modeling of various physical mechanisms, and the validation and reliability of numerical prediction, can be drawn from these studies. This is, perhaps, partially due to the difficulties in getting reliable measurements in multiphase systems. It also reflects the fact that most numerical studies used the Eulerian/Lagrangian approach and are limited to low-speed/dilute cases, while most experiments are conducted under more realistic conditions of higher gas velocity and holdup. With experimental techniques being developed and improved, it seemed that the numerical study is somewhat lagging behind. While most experiments are limited to laboratory scale, industrial needs for reliable numerical simulations of large-scale columns are real. A computer code for such simulations should be able to deal with the situations involving large gas velocity, high gas holdup, and churn turbulent flows. A key step towards this goal, we believe, is to validate the numerical results, in a quantitative way, by the currently available experimental measurements. As mentioned above, the studies of Lin et al. (1996) and Mudde et al. (1997) provided reliable and extensive data of bubbly flow between two narrowly separated plates. Their experiments can be approximately simulated by solving a set of 2-D equations. By doing so, one should be able to utilize their measurement results, both for time-averaged and for the transient properties, to validate the numerical prediction. In addition to the mean values, the comparison of the transient properties is of particular importance since it is related to the

backmixing and turbulence in the column. The testing of various physical models needed for closure can also be accomplished relatively readily in 2-D simulations, in comparison with the 3-D simulations.

In this article, we present a Eulerian/Eulerian dynamic simulation of the 2-D bubble column. The ensemble-averaged equations are used to solve the velocity and volume fraction field for both phases. A model of bubble-induced turbulent viscosity is incorporated into the momentum equations for the liquid phase. The effect of gas volume fraction on the interphase momentum exchange term is also included. The numerical predictions of the macroscopic structures and mean properties are compared with the experimental data provided by Mudde et al. (1997) and Lin et al. (1996). Our objective is to test the applicability and accuracy of the Eulerian/Eulerian method for the dynamic simulation of bubble-driven two-phase flow in 2-D bubble columns.

Model

Ensemble-averaged equations for two-phase flow

Many attempts have been made to derive the averaged equations for dispersed two-phase flows (Drew, 1983; Wallis, 1991). Either the volume averaging or the ensemble averaging technique can be used to derive the equations for the so-called two-fluid form widely used in engineering. In the recent ensemble averaging approach presented by Zhang and Prosperetti (1994, 1997), the exact Navier-Stokes equations for the continuous phase are averaged by using the phase ensemble averaging method (averaged over all the configurations such that at time t the position x is occupied by the continuous phase). For the disperse phase, a method of particle ensemble average is introduced in which global particle attributes (such as the velocity of the center of mass) are averaged directly. In other words, the averaged equations for the dispersed phase are obtained by directly ensemble averaging the equations of motion of particles where each particle is treated as a single entity.

For the incompressible liquid and gas, the continuity equations for each phase can be written as

$$\frac{\partial \epsilon_c}{\partial t} + \nabla\cdot(\epsilon_c u_c) = 0 \tag{1}$$

and

$$\frac{\partial \epsilon_d}{\partial t} + \nabla\cdot(\epsilon_d u_d) = 0 \tag{2}$$

The momentum equation for the liquid phase is written as

$$\rho_c \epsilon_c \left(\frac{\partial u_c}{\partial t} + u_c\cdot\nabla u_c \right) = \rho_c \epsilon_c g - \epsilon_c \nabla p - (M_d + M_{vm}) + \nabla\cdot(\epsilon_c \sigma_c) + \nabla\cdot\left(\epsilon_c \sigma_c^b\right) \tag{3}$$

where the stress tensor σ_c is related to the strain rate by

$$\sigma_c = \mu_c^*\left(\nabla u_c + \nabla u_c^T\right) \tag{4}$$

where $\mu_c^* (= \mu_c(1 + 5/2\,\epsilon_d + o(\epsilon_d))$ is the effective viscosity. The interphase momentum-exchange terms M_d and M_{vm} are defined as

$$M_d = \frac{6\epsilon_d \epsilon_c}{d_p^3 \pi} F_d \tag{5}$$

and

$$M_{vm} = \frac{1}{2}\epsilon_d \epsilon_c C_{vm}\, \rho_c \left(\frac{Du_c}{Dt} - \frac{Du_d}{Dt} \right) \tag{6}$$

where D/Dt represents the substantial derivative. The term $\nabla\cdot(\epsilon_c \sigma_c^b)$ is due to the bubble induced turbulence stresses, which will be elaborated later in this section. The terms M_d and M_{vm} are due to drag and added-mass force, respectively.

As derived by Zhang and Prosperetti (1994, 1997), the momentum equation for the gas phase can be obtained by ensemble averaging the equation of motion of a spherical bubble (the Newton's law) moving through fluid, which gives

$$\rho_d \epsilon_d \left(\frac{\partial u_d}{\partial t} + u_d\cdot\nabla u_d \right) = \rho_d \epsilon_d g - \epsilon_d \nabla p + (M_d + M_{vm}) \tag{7}$$

Since each bubble moves as a whole object, the rotational and the internal motion of the bubbles are neglected. As a result, a term related to the shear stress of the gas phase vanishes. Equation 7 explicitly indicates that the bubbles respond to the continuous-phase pressure, rather than to some dispersed-phase pressure. This feature of the model is in agreement with the physical intuition. The dispersed-phase pressure, that is, the pressure inside the bubble, cannot affect the motion of the bubbles directly, but only indirectly through its relation with the continuous-phase pressure resulting from the dynamic boundary conditions at the bubble surface. In the present situation there is no need to solve the momentum equation in the gas, but only to state that the gas pressure is spatially uniform inside each bubble.

For quantitative analysis, it is necessary not only to derive the correct form of these equations but also to obtain reliable estimates of the various averaged quantities, such as the viscous drag and added mass coefficients, that appear in the averaged equations. As is well known, the drag force acting on a spherical object moving at velocity u_d through a fluid with velocity u_c can be expressed as

$$F_d = \frac{1}{2}\rho_c r_p^2 C_D \pi |u_c - u_d|(u_c - u_d) \tag{8}$$

As a classical problem, the drag coefficient of a gas bubble in liquid has been extensively studied through the years. Here, we used the recent results by Tsuchiya et al. (1997). The drag coefficient of a bubble in a sufficiently contaminated system can be expressed by

$$C_D = \max\left[\frac{24}{Re}(1 + 0.15 Re^{0.687}),\ \frac{8}{3}\frac{E\ddot{o}}{E\ddot{o} + 4} f \right] \tag{9}$$

The effect of gas content is accounted for by modifying the liquid viscosity with gas holdup as ν_c/ϵ_c when calculating the

bubble Reynolds number. Likewise, the coefficient f in the second part of the Eq. 9 is for including the effect of gas holdup into the drag coefficient. Following Drew (1983), f takes the form

$$f = \left\{ \frac{1 + 17.67\epsilon_c^{9/7}}{18.67\epsilon_c^{3/2}} \right\}^2 \tag{10}$$

Additional resistance on a bubble is due to the relative acceleration of the bubble in the liquid. This is the added mass force given by Eq. 6. Generally, C_{vm} is a function of the volume fraction of the dispersed gas phase ϵ_d with a leading term of unity and it may also depend on the mass density ratio of the continuous and dispersed phase, that is, ρ_d/ρ_c, as recently proposed by Zhang and Prosperetti (1994). Biesheuvel and Spoelstra (1989) calculated C_{vm} in the dilute limit and found

$$C_{vm} = 1 + 3.32\,\epsilon_d + O\left(\epsilon_d^2\right) \tag{11}$$

Various expressions for C_{vm} were also proposed by Zuber (1964), Wijingaarden (1976), and many others. The difference is due to the different velocity distribution assumed in the calculation. For the cases being considered in the present study where the gas holdup does not exceed 10%, we expect the above first-order expressions to yield a good approximation.

To predict momentum transfer in bubbly flow, it is important to elucidate the turbulence of the continuous liquid phase. As proposed by Sato and Sekoguchi (1975) the turbulent stress in the liquid phase with bubbly flow can be subdivided into two components, one due to the inherent (shear-induced) turbulence which is independent of relative motion of the bubbles, and the other due to the additional turbulence caused by bubble agitation (bubble-induced turbulence). Experimental evidence (Lance and Bataille, 1991; Theofanous and Sullivian, 1984) indicates that, for low holdup bubbly flow, the two parts are only weakly coupled so that the linear superposition can be applied. As mentioned before, we only model the bubble-induced turbulence.

$$\boldsymbol{\sigma}_c^b = -\rho_c \overline{u'' u''} \tag{12}$$

By appling the eddy viscosity model, Sato et al. (1981) suggested

$$\boldsymbol{\sigma}_c^b = \rho_c \nu_b^t \left(\nabla u_c - \nabla u_c^T\right); \qquad \nu_b^t = k_b \epsilon_d d_p |u_c - u_d| \tag{13}$$

This model for the bubble-induced enhancement in viscosity is based on the concept of mixing length. As a fluid particle approaches a bubble with a velocity, say u_c, its velocity will obviously be distributed in contrast to the situation where the bubble is absent. If we apply the Stokes theory, this disturbance is proportional to the relative velocity between the fluid and bubble, that is, $u_c - u_d$. It is logical then to assume that this disturbance propagates over a distance of d_p, that is, the diameter of the bubble. Therefore, the momentum transfer caused by this mechanism, in addition to the shear induced one, results in the above model in which bubble diameter is taken to be the bubble-induced turbulence length scale. The empirical constant k_b usually takes a value of 1.2.

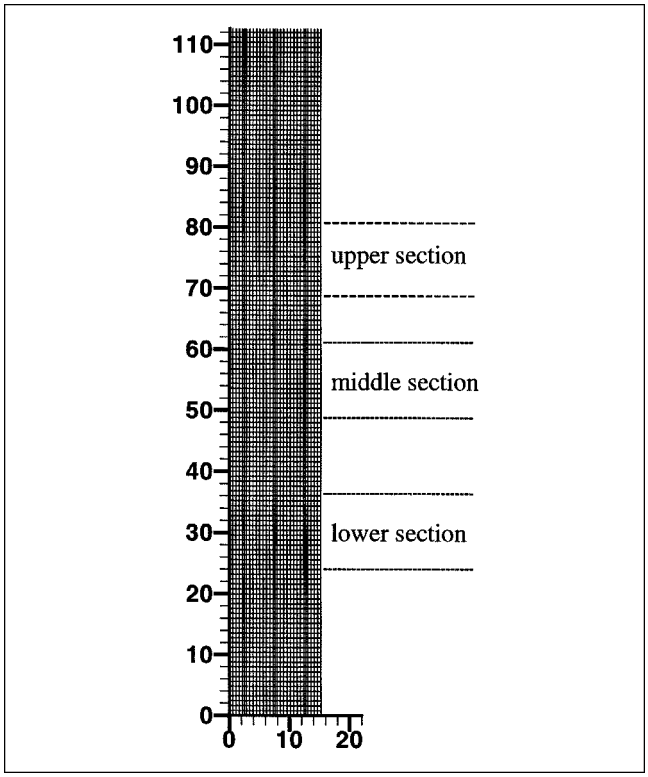

Figure 1. Mesh system for a 2-D column with discrete gas injectors.

Numerical implementation

A package CFDLIB developed by the Los Alamos National Laboratory (Kashiwa and Rauenzahn, 1994) is used for the simulations presented in this article. CFDLIB is a Fortran code library for multiphase flow simulations. It uses a cell-centered finite-volume method applied to the time-dependent equations of conservation. The methodology and numerical scheme are described by Cranfill (1983), Baumgardner et al. (1990), Addessio et al. (1992), and Kashiwa et al. (1993). Some applications can be found in Kashiwa and Rauenzahn (1994). To adopt the code to the present problem, some parts of the code related to the interphase momentum exchange and turbulence calculations are modified according to the models discussed in the last section.

Figure 1 shows the mesh system for a 15-cm wide column. The grid sizes in horizontal and vertical direction are 1.0 cm and 0.5 cm, respectively. In order to obtain better comparison with experimental data, we set the conditions for our simulations as close to those used in Mudde et al.'s (1997) experiment as possible. The flow conditions and column sizes for each run are listed in Table 1. In order to prevent overflooding, the extend of the computational domain in the z-direction is usually set to 1.2 to 1.5 times of column's static height. At the top of the column, the boundary condition is the atmospheric pressure. The gas injectors are numerically realized by setting openings at the bottom of the column which allow only the gas phase to pass through at a velocity

Table 1. Column Size and Flow Conditions*

Col. Width W (cm)	U_{sup}	Static Liquid Hgt. H (cm)	No. of Bubble Injectors	Aspect Ratio
11.2	1.0	110	2	9.8
10.16	1.22	160	2	15.8
	2.44	160	2	15.8
	3.66	160	2	15.8
	5.49	160	2	15.8
15.2	1.0	110	3	7.2
32.0	1.9	110	6	3.4

*In the experiments of Lin et al. (1996) and Mudde et al. (1997), the distance between two column walls in the third dimension is 1.27 cm.

which multiplied with gas holdup matches the value of gas superficial velocity. This was done since the size of the actual gas injectors used in the experiments (such as 0.16 cm in diameter) is too small to be resolved in the present numerical simulation. Simulated openings are about 2 to 4 times larger than the real injectors. Notice that in Figure 1 the grid is finer at the locations of gas injectors.

All simulations start from a static initial condition where the main body of the column is filled with liquid, that is, $\epsilon_c = 1$ and $\epsilon_d = 0$, up to the column's static height. Above the static height, there is gas only which corresponds to the initial condition, $\epsilon_c = 0$ and $\epsilon_d = 1$. The simulations are then performed until a quasi-steady state is reached. The time-averaged quantities are then calculated as defined in the following expressions

$$\bar{u}(x) = \frac{1}{N}\sum_{n=N_s+1}^{N+N_s} u^n(x); \qquad \bar{v}(x) = \frac{1}{N}\sum_{n=N_s+1}^{N+N_s} v^n(x) \tag{14}$$

$$\overline{u'u'} = \frac{1}{N}\sum_{n=N_s+1}^{N+N_s} u_n^2 - \bar{u}^2; \qquad \overline{v'v'} = \frac{1}{N}\sum_{n=N_s+1}^{N+N_s} v_n^2 - \bar{v}^2;$$

$$\overline{u'v'} = \frac{1}{N}\sum_{n=N_s+1}^{N+N_s} (u_n - \bar{u})(v_n - \bar{v}) \tag{15}$$

where $u_n(x)$ and $v_n(x)$ are the horizontal and vertical components of liquid velocity at time step n; N_s denotes a time step when the quasi-steady state is reached. In all simulations the velocity and gas holdup fields are sampled every 0.03–0.1 s for statistics. To ensure the convergence of the averaged quantities, the averaging processes are performed for 50 to 100 s which corresponds to a period of time during which about 10 to 20 meandering waves pass through a point at the center-line of the column. The spatial averaging is then performed along the vertical direction within the lower, middle, and upper sections as shown in Figure 1, respectively. The locations and sizes of these three sections are exactly the same as the observation windows in Mudde et al.'s (1997) experiment.

Results and Discussion

Dynamic characteristics of the large structures

Chen et al. (1989) have observed in their visual study of 2-D bubble columns that when the liquid depth exceeds the column width (when column's aspect ratio exceeds one), a central wave-like plume accompanied with two staggered rows of vortices, which resemble the Karman vortex street appear. Tzeng et al. (1993) and Lin et al. (1996) further classified the large flow structures in the 2-D bubble column into four distinct flow regions, namely the central plume region, fast bubble flow region, vortical flow region, and descending flow region. A dynamic numerical simulation should be able to capture these characteristics observed in the experiment. Figure 2 shows samples of the instantaneous flow patterns in three columns with different width, with different number of gas injectors and at different superficial gas velocities. The images are taken arbitrarily from the simulations after the dynamic stationary state is reached. The flow condition, that is, the superficial gas velocity U_{sup} (cm/s) number and location of the gas injectors, and the column size of the three cases studied match the experiments by Mudde et al. (1997). Actually, in Mudde et al.'s experiment, the dynamic heights of gas-liquid mixture for all the cases were kept at 110 cm while in the simulation the static liquid height, that is, the ungassed height, is 110 cm. Since gas holdup is very low, the differences in dynamic heights are 5%. The gray scale images show the continuous contours of gas holdup for the entire compu-

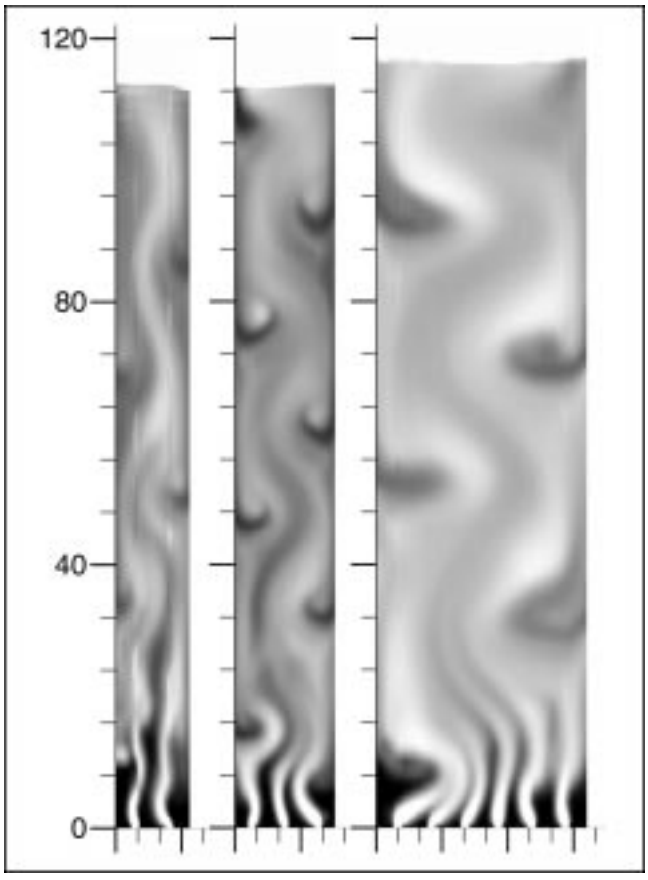

Figure 2. Instantaneous contour plots of gas holdup for 10.2 cm (left), 15.2 cm (middle), and 32 cm (right) column.

11- and 15-cm columns are operated at $U_{sup} = 1$ cm/s. 32-cm column is operated at $U_{sup} = 1.9$ cm/s. Grayscale contour legend for 11- and 15-cm column: $\epsilon_d = 0$ (black)—8% (white). For 32-cm column: $\epsilon_d = 0$ (black)—11% (white).

tational domain. The sharp change in the darkness at the upper section of the column indicates the interface between the gas liquid mixture and the all-gas section at the top of the column. As gas is injected into the column, this interface is naturally formed from the initial condition as described in the last section. Since the three columns start from the same stationary water height (110 cm), the free surface of the one with a higher superficial gas velocity U_{sup} obviously reaches a higher level due to higher gas holdup. From these visualizations, the wave-like central plume with relatively high gas concentration and the vortices adjacent to the sidewalls are clearly observed. The staggered vortices along the walls can be viewed in more detail by plotting the liquid velocity vectors. Figure 3 shows an instantaneous liquid velocity field together with the gas holdup contour plot of the 15-cm column. In the region of the central plume, the liquid moves upwards in a meandering manner. In the vortical region the vortices with alternative direction of rotation, which form the counter-rotating vortex pairs along the sidewalls, coincide with the low gas holdup region.

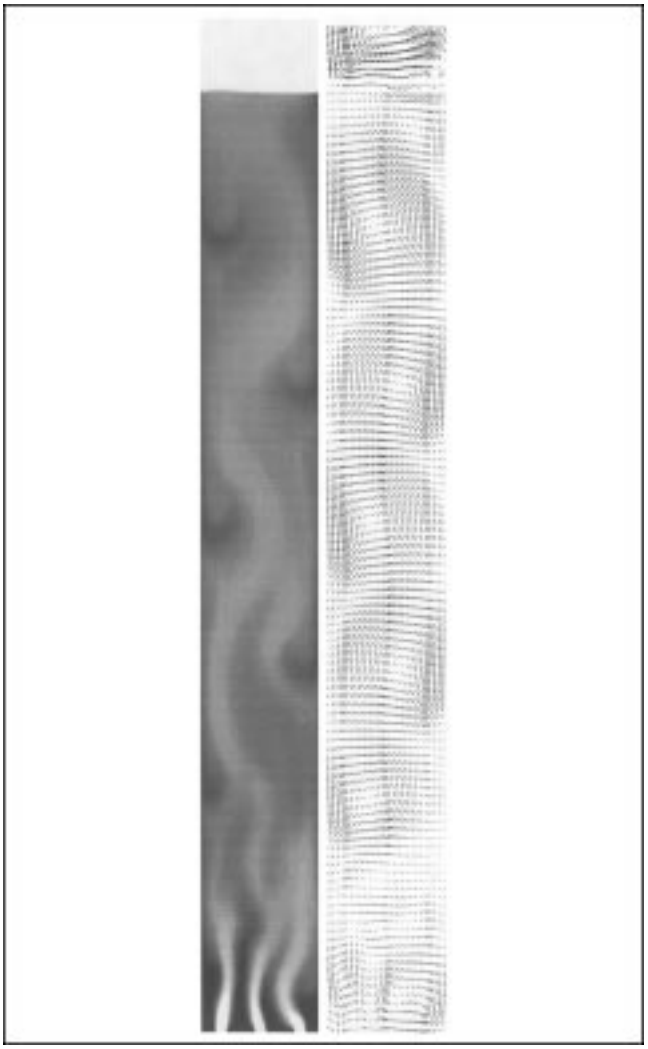

Figure 3. Instantaneous contour plots of gas holdup and liquid-velocity vectors for the 15-cm column operated at $U_{sup} = 1$ cm/s.

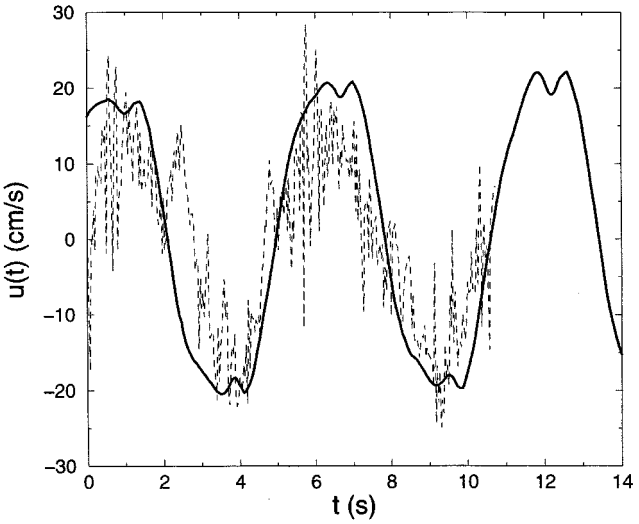

Figure 4. A time series of the horizontal liquid velocity component at the central point of the 15-cm column at $U_{sup} = 1$ cm/s.

Thick solid line is from the numerical simulation and the thin dashed line is from the PIV measurement by Mudde et al. (1997).

To study the dynamic properties of these large structures, we have performed the animations of the flow field by using the velocities and gas holdup generated from the simulations. These animations show that the bubbles injected at the bottom cluster together to move upward in a wavy manner while the vortex pairs drift down. The multiple vortex cells that are continually generated in the vortical flow region become confined by the wave motion of the central plume. The behavior of these vortices is dynamic in nature, and the formation of these vortices at each sidewall appears to be independent of each other. The entire vortex region is swinging laterally back and forth corresponding to the wave motion of the central plume.

It is of interest to determine whether the numerical simulation can produce the large structures whose primary properties match the experimental data. For this purpose, we recorded a sequence of liquid velocity with the same sampling frequency and at the same point as used by Mudde et al. (1997) in their measurement. Figure 4 compares the numerical values with data. It should be pointed out here that, in a periodical and statistically steady flow, the origin of time is irrelevant. Therefore, Figure 4 is made by shifting the numerical sequence, which is much longer than the experimental one, along the time axis so as to match one peak in both curves. One can see from Figure 4 that the numerical simulation captures the primary frequency quite well, while the high frequency contents are not resolved.

It is expected that the liquid flow in bubble columns is highly transient even at low gas velocity. Figure 5 shows a time series of liquid velocity components at the central point of the 11-cm column. The meandering nature of the central plume is clearly demonstrated by the alternation of the distinctive periods of positive and negative horizontal velocity u. Beside the primary frequency, which corresponds to the meandering structure, one can see many high frequencies and

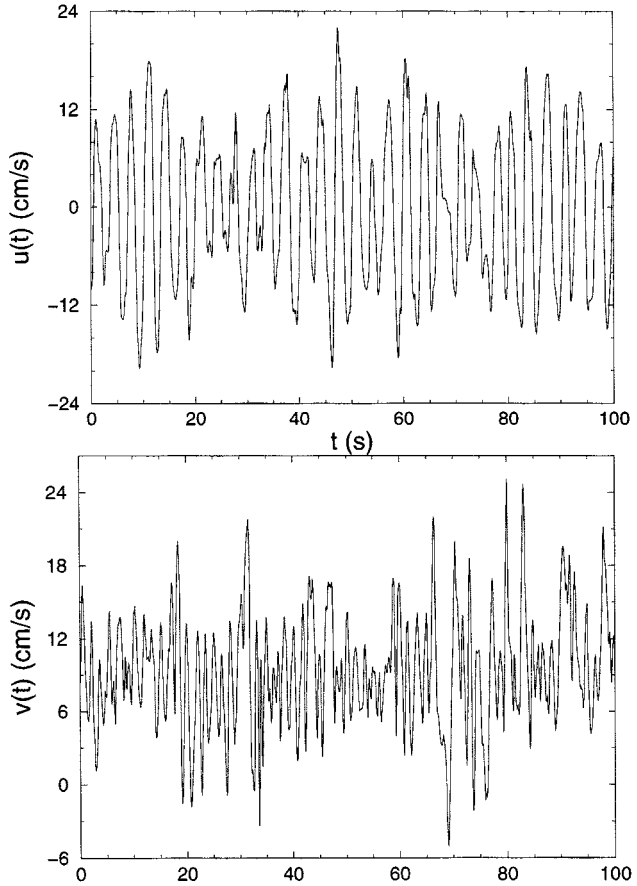

Figure 5. Time series of the liquid velocity components at the central point of the 11-cm column at $U_{sup} = 1$ cm/s.

possibly some lower frequency contents. The axial component v, on the other hand, contains more frequencies. One can have a better view on the content of time/length scale by looking at the power spectrum of the velocities, as will be shown in Figure 21. The temporal power spectra are calculated by averaging the spectra at all the points on the center line within a middle section of the 15-cm column. The spatial power spectra (not shown) are calculated by averaging the spectra of the center line over a period of 100 s. The first peak in the temporal and spatial spectrum indicates the frequency and wave length of the large structure (the meandering structure). We call these the primary frequency f_0, and the primary wave length λ_0. Beside the primary frequency and wave length, there are several smaller peaks indicating secondary frequencies and wave lengths.

Mean flow properties and comparison with experiments

To further verify our numerical results, we conducted quantitative comparisons of the mean velocity, turbulence intensities, and shear stress profiles with the experimental data provided by Mudde et al. (1997). Figure 6a shows the vertical and horizontal mean velocity profiles in the 11-cm column at $U_{sup} = 1$ cm/s. The compared profiles are for the middle section of the column where the mean flow is usually assumed 1-D. The numerical prediction of the mean horizontal velocity $\bar{u}$ is essentially zero as expected. The experimental data, however, are non-zero and exhibits an inward flow. As pointed out by Mudde et al. (1997), this is attributed to a systematic error due to the difficulty in tracking the particles in the fast-moving bubble stream and other biases. The comparison of the mean vertical velocity profile is quite good except for the near-wall region. One reason for this discrepancy is that the boundary layer is too thin to be resolved in our current simulations. By examining the measured data points near the wall, one should realize that the experiment did not resolve the wall layer either. Using the measurement of gas holdup profile reported by Reese et al. (1996), one would be able to examine to what extent the PIV data by Mudde et al. satisfy the mass balance. The numerical results do satisfy the mass balance.

The predictions for the 32-cm column are also compared with the experimental data as shown in Figure 6b. Since the window of the PIV measurement covers only half of the column, the data is provided for the left half of the column. Notice that the gas superficial velocity for this case is some-

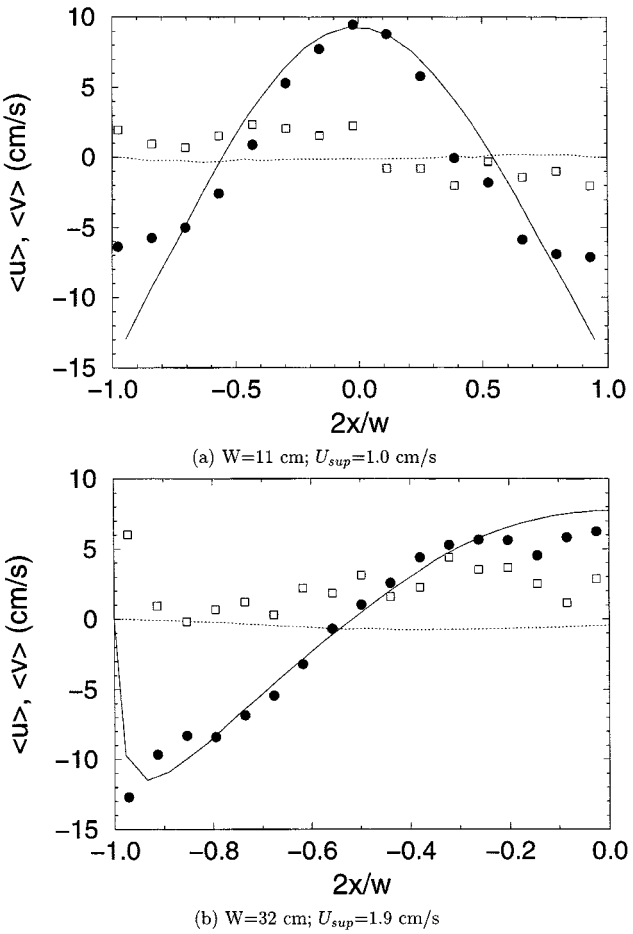

Figure 6. Time-averaged liquid velocity profiles for the 11-cm column at $U_{sup} = 1$ cm/s and the 32-cm column at $U_{sup} = 1.9$ cm/s.

—— and ···· are the numerical predictions of the vertical (axial) velocity component $\bar{v}$ and the horizontal velocity component $\bar{u}$, respectively. ● and □ represent the experimental measurements of $\bar{v}$ and $\bar{u}$, respectively. The experimental data are from Mudde et al. (1997).

what higher ($U_{sup} = 1.9$ cm/s). The comparison is satisfactory and slightly improved in the wall region.

For the 15-cm column, the comparisons of the computed and experimental determined mean vertical liquid velocity are made for the middle, lower, and upper sections, as shown in Figure 7. Again, the numerical values match the data quite well except in the wall region. The experimental profiles for the middle and upper sections are similar, while the one for the lower section is somewhat different. Mudde et al. (1997) argued that this is due to the fact that the flow is not fully developed in the lower section. The computed profiles for the three sections, on the other hand, are almost identical. Thus, the numerical values for the upper and middle sections are higher in magnitude than the experimental values. The discrepancy between the predictions and data in the near wall region may be attributed to the effect of finite thickness of the third dimension. In experimental the 2-D flow was realized between two narrowly separated plates. The distance between the plates was 1.27 cm. In the near-wall region the flow is really rather 3-D. Thus, the slowing down of fluid by the wall in third dimension, that is, the parallel plates, become significant. This effect, however, is not accounted for in the 2-D simulations. Since the thickness of the boundary layer is inversely proportional to the velocity, we would expect this type of discrepancy to be reduced as velocity increases. In fact the profiles for the lower section in Figure 7, where the velocity is high in magnitude, shows this trend. Also the results for a case of higher U_{sup} (such as Figure 6b) indicate that this may be a reasonable explanation.

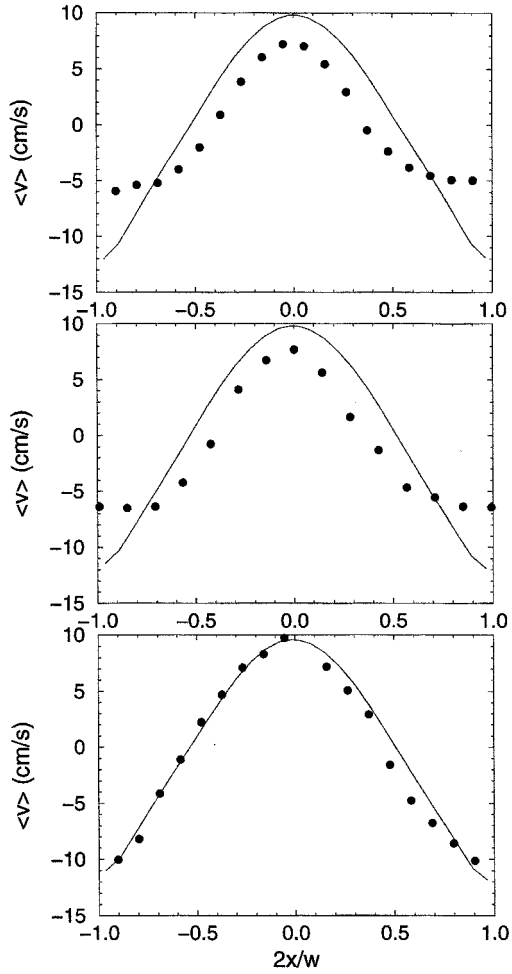

Figure 7. Averaged velocity profiles for the 15-cm column at $U_{sup} = 1$ cm/s.

Top: upper section; Middle: middle section; Bottom: lower section. — and ● represent the numerical prediction and experimental data, respectively.

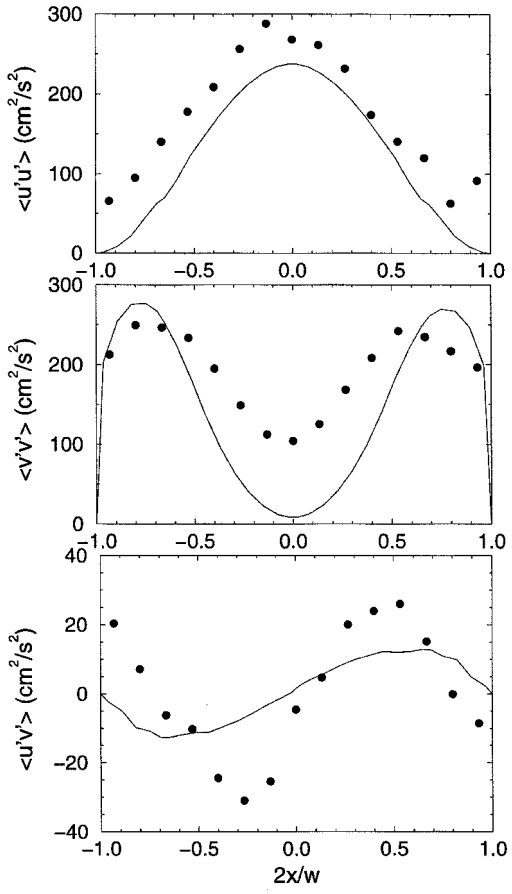

Figure 8. Time-averaged profiles of turbulence intensities and Reynolds shear stress for the middle section of the 15-cm column at $U_{sup} = 1$ cm/s.

——: Numerical values; ●: experimental data measured by Mudde et al. (1997).

The numerical predictions of turbulence intensities $\overline{u'u'}$ and $\overline{v'v'}$ and Reynolds shear stress $\overline{u'v'}$ for the 15-cm column operated at $U_{sup} = 1$ cm/s are compared with data in Figure 8. When doing such comparison, one should realize that the experimental data is the 2-D representations of a really 3-D flow field. Thus, the velocity in the third dimension may cause fluctuations in the measurement which in turn introduce some type of ''turbulence'' that contributes to non-zero Reynolds stresses in the near-wall-region. The $\overline{u'u'}$ reaches a peak at the central portion of the column since u attain its highest magnitude in the center due to the nature of the meandering motion of the central plume. The peaks of $\overline{v'v'}$ at the near-wall vortical region are consistent with the fact that the flow dynamically changes from upward to downward in such areas. Although the general trend of the numerical values match

the data, there are significant differences in values. It is clear that the simulation underpredicts the turbulence related properties. In reality, for the cases of low gas velocity, bubbles keep their identity while they rise up through the column. The drag force is thus always concentrated in the liquid surrounding the bubble. In the Eulerian/Eulerian approach, however, bubbles are not identified as single identities. Although the drag force is calculated based on the single bubble formulation, it is not confined to the region adjacent to the bubbles, as it should be; rather, it is more "dispersed" in the liquid. (This is obviously the inherent drawback of using the two-fluid model to describe two-phase flow when the dispersed phase is very dilute. One extreme example is that the Eulerian/Eulerian method cannot be used to simulate the motion of a single bubble in liquid.) The fluctuations induced by concentrated drag force are thus smoothed, which results in a lower level of turbulence intensities than what actually exists. Considering that the overall gas holdup is only a few percentages in the current simulations, it would be reasonable to expect better agreement with data when gas superficial velocity becomes higher. However, good agreement of the calculated mean velocity profile with data indicates that the effects of turbulence, here mainly the bubble-induced turbulence, are properly modeled and included in the calculation.

Figures 8 and 5 suggest that a significant part of the turbulence intensities and Reynolds shear stress are due to the large structures. The velocity field, therefore, can be thought of as consisting of three parts: the mean flow, which is time-independent, the slow wave like oscillation, which represents the large-scale meandering structure, and the part of high frequency. To study this high-frequency content, we remove the low-frequency part from the liquid velocity field and perform the time-averaging procedure on the resultant filtered flow field. The filtering procedure is achieved by first performing the Fourier transform for u and v. The Fourier coefficients which correspond to the primary frequency, which can be estimated from the power spectrum, are then set to zero. Finally, the altered velocity field in Fourier space is transformed back to the physical space. Mudde et al. (1997) processed their experimental data on a 15-cm column at 1 cm/s in a similar way. To compare with their results, we manipulate the numerical quantities for the same column at the same gas velocity. The results are shown in Figure 9. Several factors need to be pointed out. The filtered frequency for the experimental data is 0.2 Hz. For the numerical values, on the other hand, the filtered frequency, which is chosen by referring to the power spectrum as will be shown in Figure 21, is about 0.18 Hz. To be consistent with the experiment, where a single cut-off-frequency was used, here we use 0.18 Hz for both u and v. The numerical profiles are calculated by averaging the values over 100 s, which allows more than 20 waves to be recorded. The experimental profiles, however, are obtained by averaging over a time sequence of about 10 s, which contains only two waves. Mudde et al. (1997) also realized that the short averaging time period of the data is responsible for the significant discrepancies between the experimental profiles in Figure 8 and the (unfiltered) experimental profiles of Figure 9. As a result, the profiles are symmetric, while the experimental ones are not. Nevertheless, the contributions of the large structures to the turbulence related quantities are clearly indicated. As observed in the experiments and

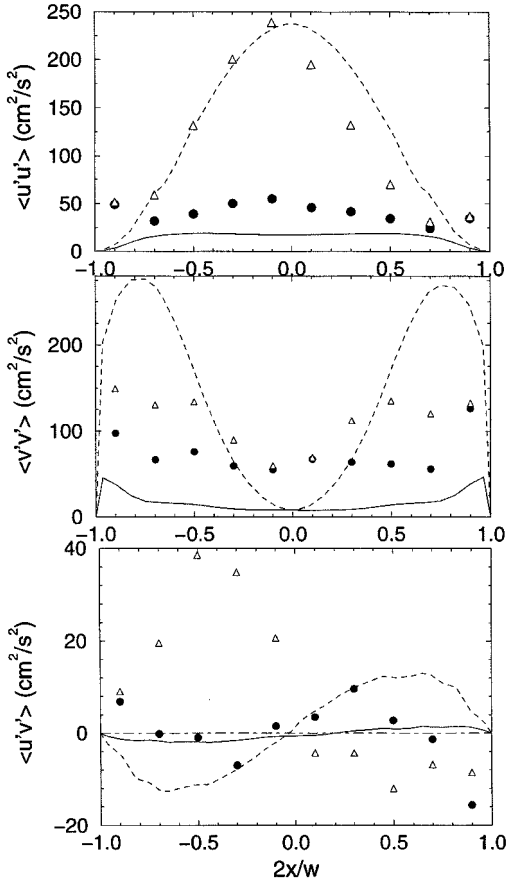

Figure 9. Time-averaged profiles of filtered and unfiltered turbulence intensities and Reynolds shear stress for the middle section of the 15-cm column at $U_{sup} = 1$ cm/s.

——: Numerical (filtered); – – –: numerical (unfiltered); ●: experimental (filtered); Δ: experimental (unfiltered). The experimental data are taken from Mudde et al. (1997).

numerical visualizations, the meandering structure results in large values of $\overline{u'u'}$ in the central region of the column. With the removal of this large structure, the filtered profile, therefore, is much lower and flat in the core region. The relatively sharp damping shape in the near-wall region is not changed much. On the other hand, the removal of the low-frequency mode which is associated with the vortices gives a largely reduced value of $\overline{v'v'}$ in the near-wall region. It seems that the large structure has relative small effect on Reynolds shear stress. Here, we have noticed that the numerical profiles of Reynolds shear stress, both unfiltered and filtered, follow the Boussinesq approximation. The unfiltered experimental Reynolds shear stress, however, does not agree qualitatively with the one given by Figure 8 which is in line with the Boussinesq approximation. This contradiction may suggest that this particular set of data by Mudde et al. (1997) is not reliable or, at least, is too crude. Even so, the comparisons illustrate that our present numerical simulation is able to capture to some extent the high-frequency/small-scale fluctuations in the turbulence bubble-driven flows.

The dynamic behavior of the large structures is characterized by the wave length and frequency of the meandering

central plume. It is expected that these quantities vary with column size and gas superficial velocity. Lin et al. (1996) have conducted an extensive and detailed experimental investigation, in 2-D columns, of this topic. They found that, in the same column, the frequency increases with gas velocity, while the wavelength decreases. At the same gas superficial velocity, the frequency decreases as the size of the column increases. The wavelength is proportional to the column size. When the wavelength and frequency are multiplied to give the vortex descending velocity, they found that it is basically a function of the superficial gas velocity only. They also found that the size of these vortices is independent of gas velocity when $U_{sup} \leq 1$ cm/s and varies with column size only.

To study the variation of large-scale structure (the frequency and wavelength) with gas velocity, we conducted a group of simulations for the 10.16 cm column. The flow conditions, as listed in Table 1, match the experiments done by Lin et al. (1996). Figure 10 shows the flow patterns when the column is operated at four different superficial gas velocities. As consistent with the experimental observation, wavelength

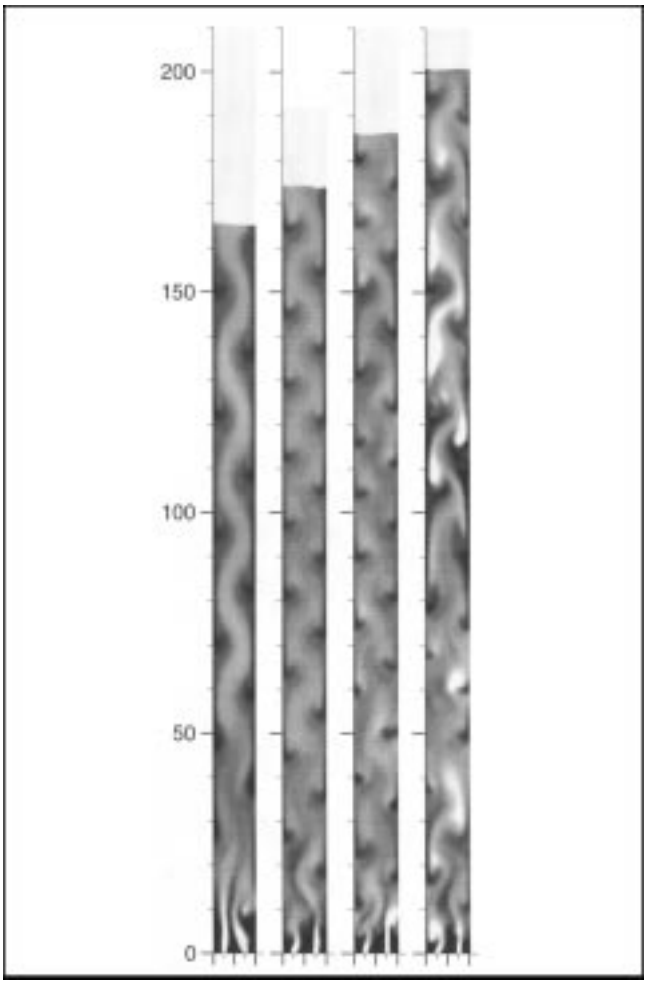

Figure 10. Instantaneous flow structures in the 10-cm column operated at different superficial gas velocity.

From the left to the right, $U_{sup} = 1.22$, 2.44, 3.66 and 5.49 cm/s.

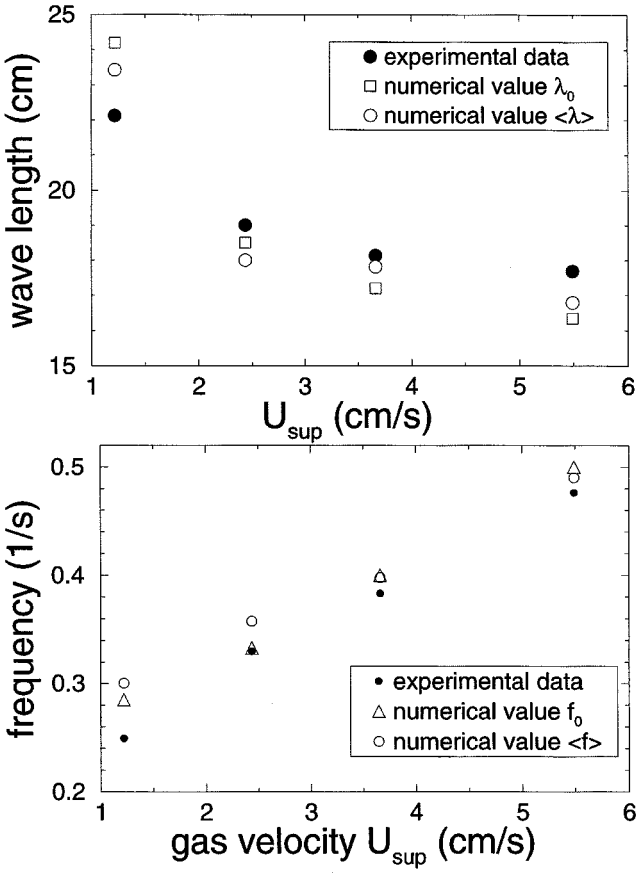

Figure 11. Frequency and wavelength of the meandering structure in a 10-cm column vs. the gas velocity.

Experimental data is taken from Lin et al. (1996).

decreases as the gas velocity increases. The overall gas holdup increases as U_{sup} increases. As the gas velocity increases, one observes intensified turbulence and the less clearly defined flow pattern.

For a quantitative comparison, we have performed each simulation for 200 s after it reached the quasi steady state and recoded all the quantities. By means of flow visualization and Fourier analysis, the averaged frequency and wavelength are calculated. Figure 11 shows the comparisons of the frequency and wavelength of the large structure with the experimentally measured values of Lin et al. (1996). The experimental values are understood to have been obtained visually as implicitly indicated in their article. We denote the frequency and wavelength of the larger structures as f_0 and λ_0. The computed values of λ_0 and f_0 are measured by the visualizations and animations of the numerically generated liquid velocity field $u_c(x,t)$. The other way to estimate the characteristics of the larger structures in a column is to calculate the mean frequency and wavelength $\bar{\lambda}$ and $\bar{f}$ as follows

$$\bar{\lambda} = \frac{\Sigma_i \lambda_i P_u(\lambda_i)}{\Sigma_i P_u(\lambda_i)} \qquad \bar{f} = \frac{\Sigma_j f_j S_u(f_j)}{\Sigma_j S_u(f_j)} \tag{16}$$

in which $P_u(\lambda)$ and $S_u(f)$ are the spatial and temporal Fourier

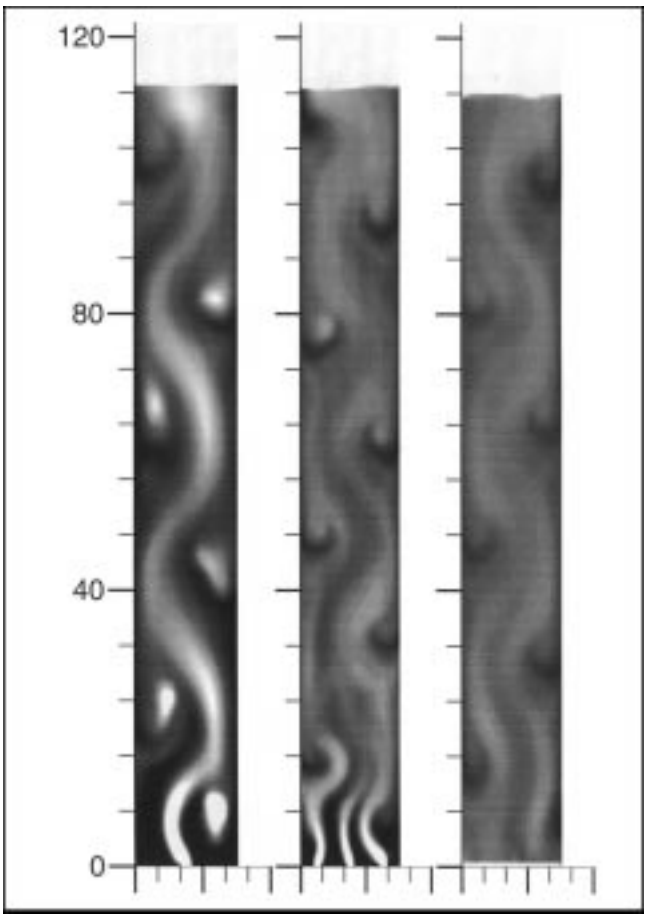

Figure 12. Instantaneous contour plots of gas holdup for the 15.2-cm columns operated at the same superficial gas velocity $U_{sup} = 1$ cm/s, but with different gas distributors: one-jet (left), three-jet (middle), and uniform (right).

The grayscale contour legend: $\epsilon_d = 0$ (black) —8% (white).

spectra for the horizontal component of the liquid velocity along the central line of the column. $\bar{\lambda}$ and $\bar{f}$ are then averaged over time and space, respectively. It can be seen that the numerical values match fairly well with the measured data particularly for the two cases of intermediate U_{sup}. We have noticed that at low and high gas velocity, the structures are not uniform over space and time, as can be seen in Figure 10. Such nonuniformity may have induced the deviations between the calculated and measured values.

Effects of gas distributors

One of the topics of interest in studying bubble columns for engineering application is the effect of a different type of gas sparger on the characteristics of the flow field and in turn on the mass/heat-transfer properties which are of great interest to chemical engineers. Numerical simulation may provide useful information in this regard. We have performed a set of simulations of the 15-cm column. Each simulation is based on a different gas distributor, consisting of one or three nozzles or a uniform gas injector. The openings are set symmetric about the centerline of the column. By uniform distributor, we mean that the gas velocity at inlet (the bottom of the column) is set to a constant single value everywhere. Among these three cases, the one with three gas injectors matches Mudde et al.'s (1997) experiments. In many bubble columns used in experiments and in industry, the gas is introduced into the column through many tiny holes on a perforated plate or even sintered plate. The size of these holes in a perforated plate is usually of the order of 10^{-1} mm. The holes are distributed uniformly on the plate. A perforated plate, whose open area is about 0.1% of the total area, would have hundreds of holes. A uniform distribution of gas velocity and volume fraction at the bottom is a reasonable inlet boundary condition for simulation of such a distributor.

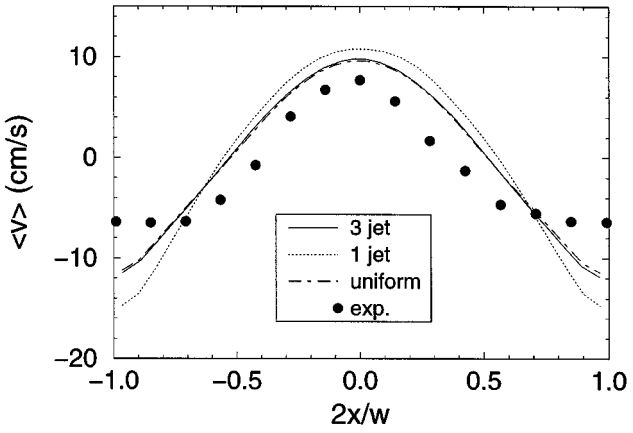

Figure 13. Time-averaged liquid velocity profiles for the 15-cm column at $U_{sup} = 1$ cm/s.

Lines represent the results of the numerical simulations with different gas distributors. Symbols represent the experimental data measured by Mudde et al. (1997) taken with three injectors.

In the cases simulated, while the gas is injected in a different way into the column, the superficial gas velocity is kept the same for all the runs. Figure 12 shows the flow pattern for these three cases. One notices first that the overall gas holdup for each case is the same. This indicates that the overall gas holdup is not affected by the gas distributors and depends on the gas superficial velocity U_{sup} only. We can see that the wavelengths of the meandering structure in columns with different types of gas distributor are very similar. The gas-rich central plume becomes wider as the number of gas injectors increases.

The profiles of the mean liquid axial velocity for the middle section of the columns are shown in Figure 13. As expected, the profile becomes less steep as the type of gas distributor approaches uniform distribution. In fact the profile for three-injector is almost identical to the one for uniform distribution. Figure 14 shows the turbulence intensities and Reynolds shear stress profiles. The column with a single gas injector, in comparison with the columns of three-jets and uniform distribution, produces much higher turbulence, as shown by the profiles for $\overline{u'u'}$ and $\overline{v'v'}$. The profiles of Reynolds shear stress $\overline{u'v'}$ indicate that, in the column with a single injector, the two components of liquid velocity, u and v, are more closely correlated than those in the other columns. This fact simply means that the liquid flow in a single-injector column is more dominated, in contrast to the column with

distributed injectors, by the coherent large structures. A visual observation on the instantaneous flow pattern, as shown in Figure 12, supports this conclusion as well.

Figure 15 shows the power spectra of the horizontal x-component of liquid velocity. The shifting of the peaks for the single-jet towards higher frequency indicates that the gas distributor can have an impact on the oscillation of the meandering structure. As shown by Lin et al. (1996), the vortex descending velocity is proportional to the wavelength and frequency. The increase in wavelength and frequency, therefore, gives rise to larger negative axial velocity at the near-wall region as shown in Figure 13. The peaks for the three-jet and uniform distributor occur at the same frequency. However, the band of the peak for the uniform distributor is wider than that for the three-jet, which indicates that more frequency content can be brought into the large structure by injecting gas uniformly. Also, the enhancement in turbulence intensities in the horizontal direction, as the gas distribution changes from three jets to uniform, as shown in Figure 14, is consistent with the widening of the peak in the power spectra. These observations suggest that the way by which the gas is introduced may affect the dispersion and mixing in the column operated in the bubbly flow regime.

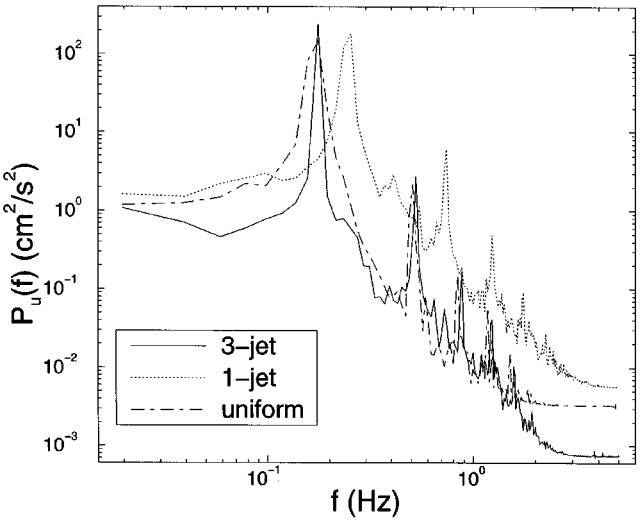

Figure 15. Temporal power spectrum of the horizontal component of the liquid velocity for the 15-cm column at $U_{sup} = 1$ cm/s with different gas distributions.

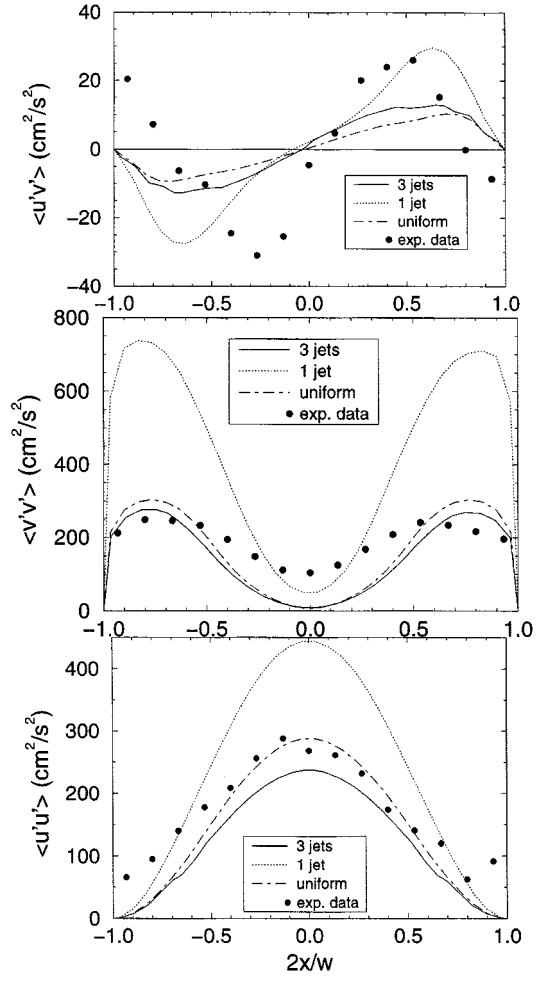

Figure 14. Time-averaged profiles of turbulence intensities and Reynolds shear stress of the liquid phase for the middle section of the 15-cm column at $U_{sup} = 1$ cm/s.

Lines represent the numerical predictions with different gas distributors: ——: three-jet; · · · ·: one-jet; —·—: uniform. ● represents the experimental data measured by Mudde et al. (1997).

Verification of physical models

As is well known, how to model the interphase momentum exchange and multiphase turbulence are, among many others, the important and controversial issues in numerical study of multiphase flow by the Eulerian/Eulerian method. In our present study, we adopted a model proposed by Sato et al.

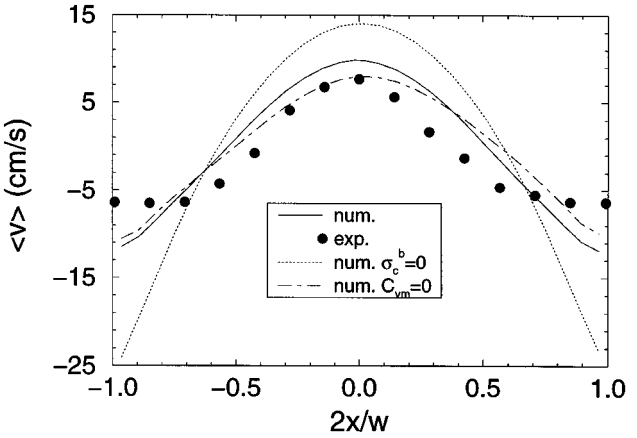

Figure 16. Time-averaged profiles of the vertical velocity for the 15-cm column at $U_{sup} = 1$ cm/s.

Lines represent the numerical predictions with different physical models. ● represents experimental data of Mudde et al. (1997).

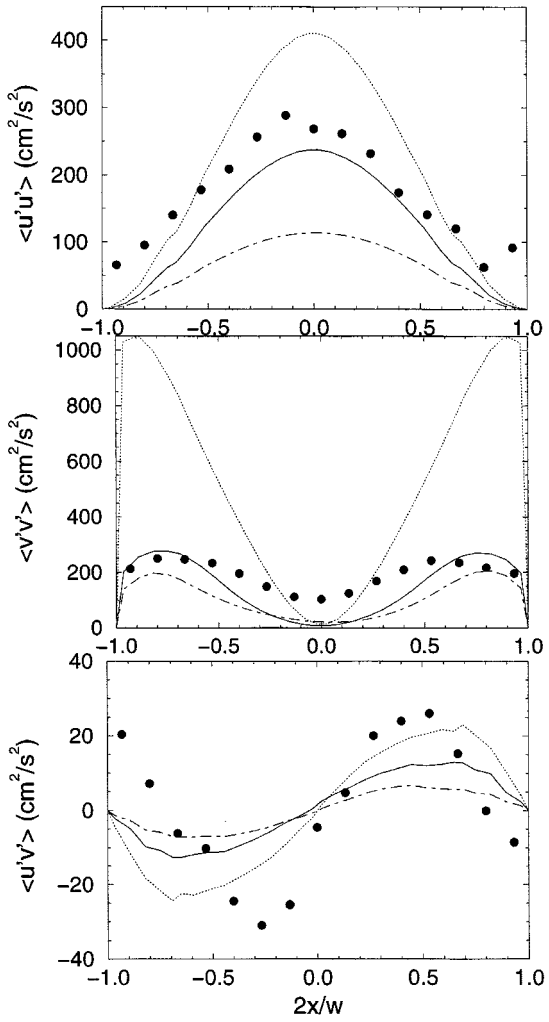

Figure 17. Time-averaged profiles of turbulence intensities and Reynolds shear stress for the middle section of the 15-cm column at $U_{sup} = 1$ cm/s.

Lines represent the numerical predictions with different physical models: ——: with bubble induced viscosity σ_c^b and added mass force; · · · ·: $\sigma_c^b = 0$; —·—: without added mass force. ● represents experimental data of Mudde et al. (1997).

(1981), as shown by Eq. 13, to account for the effect of the bubble-induced turbulence. We also include the added mass force, beside the drag force, into the interphase momentum exchange. It is therefore logical and prudent to conduct a sensitivity study of these terms. Again, we choose to simulate the 15-cm column at $U_{sup} = 1$ cm/s where the experimental data exist for comparison. The simulations are made by, respectively, turning off the bubble-induced viscosity and the added mass coefficient one at a time. Figures 16 and 17 show the profiles for axial mean liquid velocity and turbulence related average quantities, respectively. It is clear that the bubble-induced viscosity has a big effect, whereas the effect of the added-mass force is relatively small, but still not insignificant. If the power spectra, as shown in Figure 18, is examined, the effect of neglecting the bubble-induced viscosity on the macrostructure is to increase the frequency of the wavy motion. Neglecting the bubble-induced viscosity would make the liquid less viscous and, thus, results in enhancement of turbulence. It should be noticed that among the three cases simulated, the one which includes both the bubble-induced viscosity and the added-mass force matches the experimental data best. We may, therefore, conclude that our present model includes the key physical mechanisms and gives a reasonable prediction of gas-liquid flow in 2-D bubble column.

In the present model of the drag force a single value of bubble size is assumed. Actually, the bubble size is the only adjustable parameter in the model. Throughout this article, we use 0.5 cm in diameter as the bubble size, simply because the bubbles of this size were mostly observed by Lin et al. (1996) and Mudde et al. (1997) in their PIV experiments. In order to examine the sensitivity of these results to the bubble size, we repeated the simulation of the 15-cm column by using two other bubble sizes of 0.8 cm and 0.25 cm. The axial mean velocities and turbulence properties for the three cases are compared. It is interesting and somewhat surprising to find that changing the bubble size by a factor of 3.2 does not greatly affect the results. However, we have also found in our simulations that, if one uses too large a bubble size, the liquid will not start to circulate. Since the bubble size is inversely proportional to the amount of drag force per unit volume of liquid, there must be a threshold below which the liquid simply does not gain enough momentum to move.

Effects of numerical resolution and boundary conditions

One of the critical issues in numerical simulation is the effect of the mesh size and type. Although the scope of this article is to use the Eulerian/Eulerian method as implemented in CFDLIB, it is always wise to check the effect of the numerical resolution. We used three different meshes, as listed in Table 2, for the simulations of 15-cm column at U_{sup}

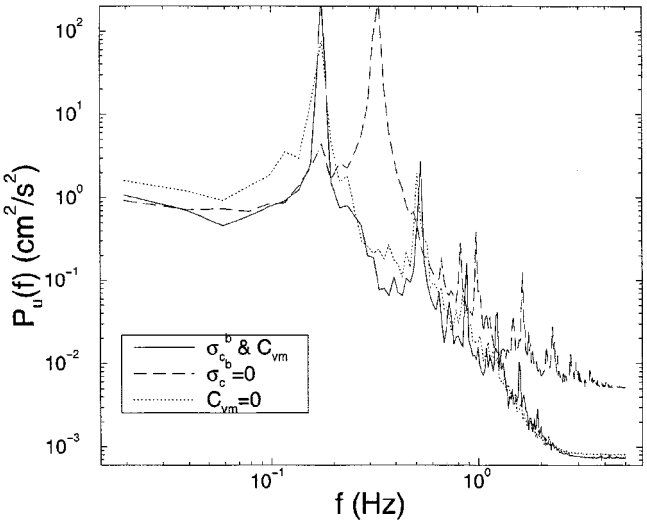

Figure 18. Temporal power spectrum of the transverse component of the liquid velocity by different physical models.

Case is a 15-cm column at $U_{sup} = 1$ cm/s.

Table 2. Spatial Resolution for the Simulation of 15-cm Column

Mesh	I (Medium)	II (High)	III (Low)
Δx (cm)	0.55	0.38	0.85
Δy (cm)	1.0	0.75	1.2
Δx_1 (cm)	0.32	0.24	0.32
Δy_1 (cm)	1.0	0.75	1.2

*Δx_1 and Δy_1 are the mech sizes in the jet region.

$= 1$ cm/s. Figure 19 shows the computed axial mean velocity using different meshes. Differences are definitely present, especially in the wall region. However, the difference in the computed values throughout most of the column are acceptable for most engineering calculations. In the wall region, the computed velocity values approach the experimental data in monotonic fashion as mesh is refined. Figure 20 shows the turbulence intensities and Reynolds shear stress. The differences in calculated values are now much larger especially for the transverse component of turbulent intensities $\overline{u'u'}$. It seems that $\overline{u'u'}$ is enhanced as the mesh becomes finer. The effect of the mesh on the dynamic properties of the flow field can be examined by looking at the power spectra of the liquid velocity components. Figure 21 shows the power spectra of the liquid velocity component u. It is seen that primary frequency shifts towards the low value and more higher-frequency contents are resolved, as the mesh is refined. By recalling Figure 11, where the primary frequencies are overestimated by the numerical simulation, one would expect an improvement of such a calculation when a finer mesh is used. However, the issue of accuracy of the computed turbulence quantities as a function of mesh size remains. An extensive study is needed to determine whether convergent behavior is obtained. This was not our objective as we focused on the physical models included in the simulations.

Finally, we studied the effect of different boundary conditions on the computed quantities. With regard to the boundary conditions in gas-liquid flow, the most common practice is to assume the no-slip condition for the liquid phase and free-slip condition for the gas phase at the vessel wall. The latter is due to the assumption that the gas, being in the form of bubbles, is able to slip along the solid wall. If the gas phase is treated as a continuum, as is the case in the Eulerian/Eulerian approach, the no-slip condition can also be applied. Since the boundary layer is very thin in most cases, it is also of interest to test the effect of the free-slip boundary condition for the liquid phase. The simulations were made for the 15-cm column at $U_{sup} = 1$ cm/s by applying different boundary conditions (free-slip or no-slip) for liquid and gas phase, respectively. The results confirm that no-slip for liquid phase and free-slip for gas phase is the appropriate boundary condition set.

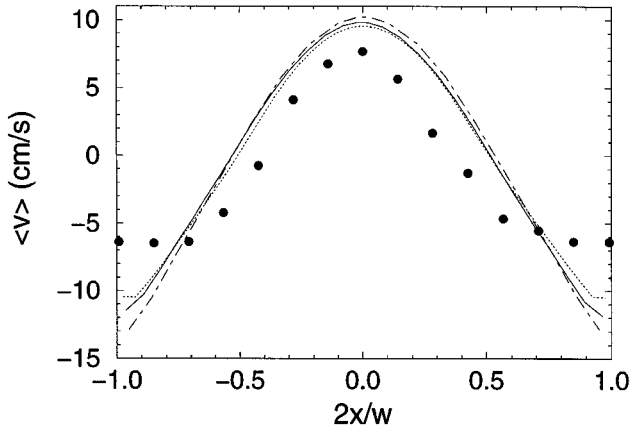

Figure 19. Time-averaged liquid velocity profiles for the 15-cm column at $U_{sup} = 1$ cm/s.

Lines represent the results of the numerical simulations with different spatial resolutions. —: Mesh I; · · · ·: Mesh II; −·−: Mesh III. ● represents experimental data measured by Mudde et al. (1997).

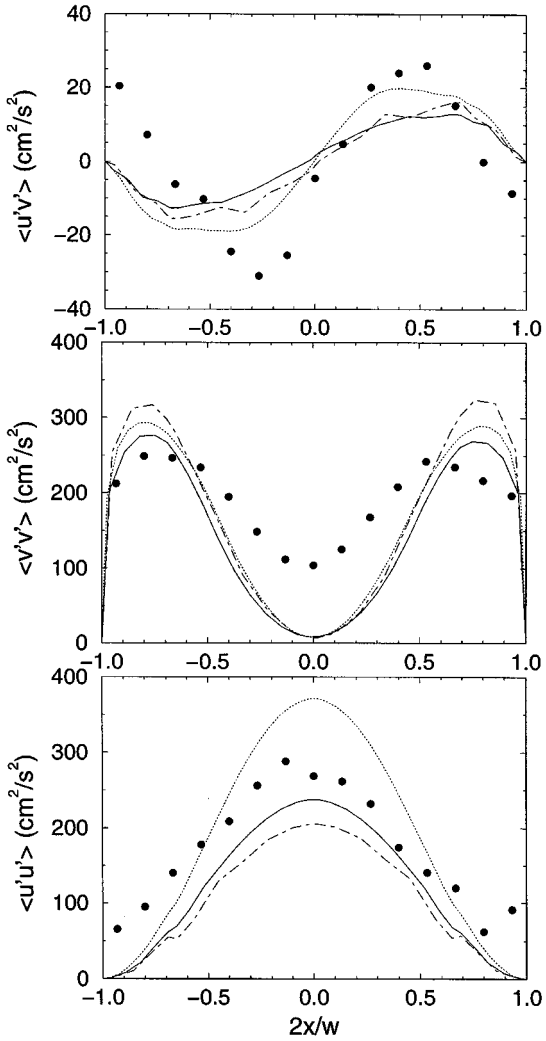

Figure 20. Time-averaged profiles of turbulence intensities and Reynolds shear stress of the liquid phase for the middle section of the 15-cm column at $U_{sup} = 1$ cm/s.

Lines represent the numerical predictions with different spatial resolutions: ——: Mesh; · · · ·: Mesh II; −·—: Mesh III. ● represents the experimental data measured by Mudde et al. (1997).

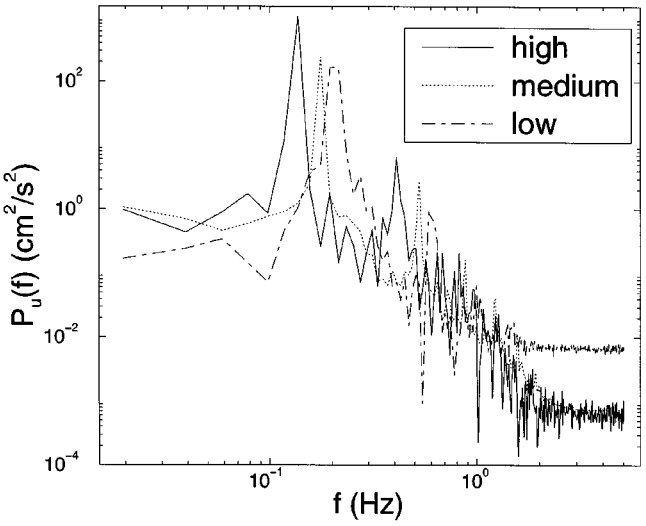

Figure 21. Temporal power spectrum of the horizontal component of the liquid velocity from the simulations using different mesh-resolutions.

Case is a 15-cm column at $U_{sup} = 1$ cm/s.

Summary and Conclusions

The numerical simulation of gas-liquid flow in 2-D bubble columns using the Eulerian/Eulerian two-fluid model is able to capture the characteristics of coherent large structures. Quantitative comparisons with the experimental data demonstrate that, by applying simple models of interphase momentum transfer and bubble-induced turbulent viscosity in the liquid phase, the two-fluid simulations are able to provide satisfactory quantitative results for mean axial velocity, as well as order of magnitude results for the turbulence intensities and Reynolds shear stress for the cases of dispersed bubbly flow. The accuracy of predicted mean liquid velocity in a 15-cm column operated at $U_{sup} = 1$ cm/s is within 15% in most of the column. The computed horizontal component of turbulence intensity in the liquid phase underestimates the experimental data by about 20%. The radial profile of the calculated axial component of turbulence intensity has the same shape as the data. The numerical values are smaller than the data by about 10% in the wall region and by 20% to 5 times in the central region. The calculated Reynolds shear stress follows the Boussinesq approximation as does the experimental one, but the former is much smaller than the latter in most of the column. The computed dynamic properties of the larger structure, that is, the wave length and frequency of the central meandering plume, and the descending speed of near-wall vortices, also agree well with the PIV measurements. The deviations between the computed and measured values of the wavelength and frequency are within 10%. Such macrostructures account for about 90% of total turbulence intensities and Reynolds stress. The importance of including the bubble-induced viscosity into the continuous phase, here the liquid, is also demonstrated. The study of the effect of the gas distributor shows that changing the bubble injector arrangements may result in significant differences in flow properties, which could affect the dispersion of passive scalars in both phases.

Acknowledgments

This work was supported by the grant from the University Coal Research (UCR) of the Dept. of Energy (DE-FG22-95PC95212). Two of the authors (Y. P. and M. P. D.) also are thankful for the companion contract from the Dept. of Energy (DE-FC22-95PC95051) which allowed the completion of this manuscript. The authors express their gratitude to Dr. Bill Heards at Exxon Research and Engineering Company and Professor S. Sundaresan at Princeton University for several constructive suggestions and discussions of the present problem and techniques used. We also thank the Los Alamos National Laboratory for providing CFDLIB to the Chemical Reaction Engineering Laboratory (CREL) at Washington in St. Louis where this work was performed.

Notation

C_D = drag coefficient
C_{vm} = virtual mass coefficient
d_p = bubble diameter, cm
Eo = Eötvös number ($\equiv g\rho_c d_p^2/\tau$)
g = gravitational constant, cm/s^2
Re = bubble Reynolds number ($= d_p|u_c - u_d|\rho_c/\mu_c$)
u_c = liquid velocity field, cm/s
u_d = gas velocity field, cm/s
ϵ_c = liquid volume fraction
ϵ_d = gas volume fraction
μ_c = liquid viscosity, gram/(cm·s)
ν_c = liquid kinematic viscosity, cm^2/s
ρ_c = liquid density, gram/cm^3
ρ_d = gas density, gram/cm^3
τ = surface tension, gram/s^2

Literature Cited

Addessio, F. L., J. R. Baumgardner, J. K. Dukowicz, N. L. Johnson, B. A. Kashiwa, R. M. Rauenzahn, and C. Zemach, ''CAVEAT: A Computer Code for Fluid Dynamics Problems with Large Distortion and Internal Slip,'' Los Alamos Nat. Lab. Report LA-10613-MS, Rev. 1, Los Alamos, NM (1992).

Baumgardner, J. R., M. C. Cline, N. L. Johnson, and B. A. Kashiwa, ''CFDLIB: A Library of Computer Codes for Problems in Computational Fluid Dynamics,'' Los Alamos Nat. Lab. Report LA-UR-90-1361 (1990).

Becker, S., A. Sokolichin, and G. Eigenberger, ''Gas-Liquid Flow in Bubble Columns and Loop Reactors: II. Comparison of Detailed Experiments and Flow Simulations,'' *Chem. Eng. Sci.*, **49**, 5747 (1994).

Biesheuvel, A., and S. Spoelstra, ''The Added Mass Coefficient of a Dispersion of Spherical Gas Bubbles in Liquid,'' *Int. J. Multiphase Flow*, **15**, 911 (1989).

Chen, J. J. J., M. Jamialahmadi, and S. M. Li, ''Effect of Liquid Depth on Circulation in Bubble Columns: a Visual Study,'' *Chem. Eng. Res. Des.*, **67**, 203 (1989).

Chen, R. C., and L.-S. Fan, ''Particle Image Velocimetry for Characterizing the Flow Structure in Three-Dimensional Gas-Liquid-Solid Fluidized Beds,'' *Chem. Eng. Sci.*, **47**, 3615 (1992).

Chen, R. C., J. Reese, and L.-S. Fan, ''Flow Structure in Three-Dimensional Bubble Column and Three-Phase Fluidized Beds,'' *AIChE J.*, **40**, 1093 (1994).

Cranfill, C. W., ''EOSPAC: A Subroutine Package for Accessing the Los Alamos Sesame EOS Data Library,'' Los Alamos Nat. Lab. Report LA-9728-M, UC-32, Los Alamos, NM (1983).

Delnoij, E., F. A. Lammers, J. A. M. Kuipers, and W. P. M. van Swaaij, ''Dynamic Simulation of Dispersed Gas-Liquid Two-Phase Flows Using a Discrete Bubble Model,'' *Chem. Eng. Sci.*, **52**, 1429 (1997a).

Delnoij, E., J. A. M. Kuipers, and W. P. M. van Swaaij, ''Computational Fluid Dynamics Applied to Gas-Liquid Contactors,'' *Chem. Eng. Sci.*, **52**, 3623 (1997b).

Delnoij, E., J. A. M. Kuipers, and W. P. M. van Swaaij, ''Dynamic Simulation of Gas-Liquid Two-Phase Flow: Effect of Column As-

pect Ratio on the Flow Structure,'' *Chem. Eng. Sci.*, **52**, 3759 (1997c).
Devanathan, N., D. Moslemian, and M. P. Duduković, ''Flow Mapping in Bubble Columns Using CARPT,'' *Chem. Eng. Sci.*, **45**, 2285 (1990).
Devanathan, N., M. P. Duduković, A. Lapin, and A. Lübbert, ''Chaotic Flow in Bubble Column Reactors,'' *Chem. Eng. Sci.*, **50**, 2661 (1995).
Drew, D. A., ''Mathematical Modeling of Two-Phase Flow,'' *Ann. Rev. Fluid Mech.*, **15**, 261 (1983).
Kashiwa, B. A., N. T. Padial, R. M. Rauenzahn, and W. B. VanderHeyden, ''A Cell-Centered ICE Method for Multiphase Flow Simulations,'' Los Alamos Nat. Lab. Report LA-UR-93-3922 (1993).
Kashiwa, B. A., and R. M. Rauenzahn, ''A Multimaterial Formalism,'' FED, 185, *Numerical Methods in Multiphase Flows*, ASME, New York, 149 (1994).
Lance, M., and J. Bataille, ''Turbulence in the Liquid Phase of a Uniform Bubbly Air-Water Flow Model for Bubbly Two-Phase Flow,'' *J. Fluid Mech.*, **22**, 95 (1991).
Lapin, A., and A. Lubbert, ''Numerical Simulation of the Dynamics of Two-Phase Gas-Liquid Flows in Bubble Columns,'' *Chem. Eng. Sci.*, **49**, 3361 (1994).
Lin, T.-J., J. Reese, T. Hong, and L.-S. Fan, ''Quantitative Analysis and Computation of Two-Dimensional Bubble Columns,'' *AIChE J.*, **42**, 301 (1996).
Lopez de Bertodano, M., R. T. Lahey, Jr., and O. C. Jones, ''Development of $\kappa-\epsilon$ Model for Bubbly Two-Phase Flow,'' *ASME J. of Fluids Engineering*, **116**, 128 (1994).
Mudde, R. F., D. J. Lee, and L.-S. Fan, ''Role of Coherent Structures on Reynolds Stresses in a 2-D Bubble Column,'' *AIChE J.*, **43**, 913 (1997).
Prosperetti, A., and D. Z. Zhang, ''Disperse Phase Stress in Two-Phase Flow,'' *Chem. Eng. Comm.*, **141-142**, 387 (1994).
Reese, J., R. F. Mudde, D. J. Lee, and L.-S. Fan, ''Analysis of Multiphase Systems through Particle Image Velocimetry,'' *AIChE Symp. Ser. 310*, 92 (1996).
Sato, Y., and K. Sekoguchi, ''Liquid Velocity Distribution in Two-Phase Bubble Flow,'' *Int. J. Multiphase Flow*, **2**, 79 (1975).
Sato, Y., M. Sadatomi, and K. Sekoguchi, ''Momentum and Heat Transfer in Two-Phase Bubble Flow I,'' *Int. J. Multiphase Flow*, **7**, 167 (1981).
Sokolichin, A., and G. Eigenberger, ''Gas-Liquid Flow in Bubble Columns and Loop Reactors: I. Detailed Modeling and Numerical Simulation,'' *Chem. Eng. Sci.*, **49**, 5735 (1994).
Theofanous, T. G., and J. Sullivian, ''Turbulence in Two-Phase Disperse Flow,'' *J. Fluid Mech.*, **116**, 343 (1984).
Tsuchiya, K., A. Furumoto, L.-S. Fang, and J. Zhang, ''Suspension Viscosity and Bubble Rise Velocity in Liquid-Solid Fluidized Beds,'' *Chem. Eng. Sci.*, **52**, 3053 (1997).
Tzeng, J. W., R. C. Chen, and L.-S. Fan, ''Visualization of Flow Characteristics in a 2-D Bubble Column and Three-Phase Fluidized Bed,'' *AIChE J.*, **39**, 733 (1993).
Wallis, G. B., ''The Averaged Bernoulli Equation and Macroscopic Equations of Motion for the Potential Flow of Two-Phase Dispersion,'' *Int. J. Multiphase Flow*, **17**, 683 (1991).
Webb, C., F. Que, and P. R. Senior, ''Dynamics Simulation of Gas-Liquid Dispersion Behavior in a 2-D Bubble Column Using a Graphics Mini-Super Computer,'' *Chem. Eng. Sci.*, **47**, 3305 (1992).
Wijingaarden, L. van, ''Hydrodynamics Interactions Between Gas Bubbles in Liquid,'' *J. Fluid Mech.*, **77**, 27 (1976).
Yang, Y. B., N. Devannathan, and M. P. Dudukovic, ''Liquid Backmixing in Bubble Columns via Computer-Automated Radioactive Particle Tracking (CARPT),'' *Exp. Fluids*, **16**, 1 (1993).
Zhang, D. Z., and A. Prosperetti, ''Averaged Equations for Inviscid Disperse Two-Phase Flow,'' *J. Fluid Mech.*, **267**, 185 (1994).
Zhang, D. Z., and A. Prosperetti, ''Momentum and Energy Equations for Disperse Two-Phase Flows and Their Closure for Dilute Suspensions,'' *Int. J. Multiphase Flow*, **23**, 425 (1997).
Zuber, N., ''On the Dispersed Two-Phase Flow in the Laminar Regime,'' *Chem. Eng. Sci.*, **19**, 897 (1964).

Manuscript received Apr. 20, 1999, and revision received Sept. 15, 1999.